elongation as well as inverse aspect ratio can have significant effects on the frequencies of the resonant cavity modes.

REFERENCES

[1] M. Brambilla and U. Finzi, "Electro-magnetic eigenmodes of the toroidal cavity," *IEEE Trans. Plasma Sci.,* vol. PS-2, pp. 112–114, Sept. 1974.

[2] F. Cap and R. Deutsch, "Toroidal resonators for electromagnetic waves," *IEEE Trans. Microwave Theory Tech.,* vol. MTT-28, pp. 700–703, July 1980.

[3] J. Lileg, R. Schnizer, and R. Keil, "Perturbation theoretic computation of toroidally uniform modes within an empty torus," *AEU,* pp. 359–365, 1983.

[4] M. S. Janaki and B. Dasgupta, "Eigenmodes for electromagnetic waves propagating in a toroidal cavity," *IEEE Trans. Plasma Sci.,* vol. 18, pp. 78–85, Feb. 1990.

[5] R. Keil, "Numerical calculation of electromagnetic toroidal resonators," *AEU.* pp. 30–36. 1984.

[6] F. Cap, "Toroidal resonators and waveguides of arbitrary cross-section," *IEEE Trans. Microwave Theory Tech.,* vol. MTT-29, pp. 1053–1057, 1981.

[7] F. Cap and N. Schupfer, "Three-dimensional electromagnetic modes in magnetized toroidal plasmas," *Plasma Phys. Cont. Fusion,* vol. 31, pp. 11–19, 1989.

[8] H. M. Wu, R. Carrera, J. Dong, and M. E. Oakes, "Resonant mode analysis in toroidal cavities with elliptical cross-sections," *IEEE Trans. Plasma Sci.,* vol. 20, pp. 19–23, Feb. 1992.

[9] R. Grauer and E. Rebhan, "Analysis of ideal mhd equilibrium and axisymmetric stability for finite aspect ratio tokamaks with elliptic cross-section and flat current profile," *J. Plasma Phys.,* vol. 32, pp. 99–117, 1984.

[10] N. W. McLachlan, *Theory and Applications of Mathieu Functions.* Oxford: Clarendon, 1947.

[11] F. Cap and R. Deutsch, "Toroidal resonators for electromagnetic waves," *IEEE Trans. Microwave Theory Tech.,* vol. MTT-26, pp. 478–486, July 1978.

[12] J. G. Kretzschmar, "Wave propagation in hollow conducting elliptical waveguides," *IEEE Trans. Microwave Theory Tech.,* vol. MTT-18, pp. 547–554, Sept. 1970.

[13] F. A. Alhargan and S. R. Judah, "Tables of normalized cutoff wavenumbers of elliptic cross-section resonators," *IEEE Trans. Microwave Theory Tech.,* vol. 42, pp. 333–338, Feb. 1994.

BiCG-FFT T-Matrix Method for Solving for the Scattering Solution from Inhomogeneous Bodies

J. H. Lin and W. C. Chew

***Abstract*—A BiCG-FFT T-Matrix algorithm is proposed to efficiently solve three-dimensional scattering problems of inhomogeneous bodies. The memory storage is of $O(N)$ (N is the number of unknowns) and each iteration in BiCG requires $O(N \log N)$ operations. A good agreement between the numerical and exact solutions is observed. The convergence rate for lossless and lossy bodies of various sizes are shown. It is also demonstrated that the matrix condition number for fine grids is the same as that for coarse grids.**

Manuscript received November 17, 1994; revised March 20, 1996.

The authors are with the Electromagnetics Laboratory, Department of Electrical and Computer Engineering, University of Illinois, Urbana, IL 61801 USA.

Publisher Item Identifier S 0018-9480(96)04720-5.

I. INTRODUCTION

The scattering of electromagnetic fields by inhomogeneous bodies is a research topic that finds applications in many fields. In this paper, we propose a method of solving the inhomogeneous body problem by approximating the inhomogeneous body with small dielectric cubes. The dielectric cubes are then approximated by equivolume spheres [1]–[6]. In this manner, the T matrix [7], [8] of each individual sphere can be found in closed form. A set of linear algebraic equations can be easily derived to solve for the scattering amplitudes from each of the spheres. By using this T-matrix formulation, the Green's function singularity problem is avoided, while other formulations, such as the method of moments [9], such a singularity has to be handled with caution [10]–[12].

Direct solvers such as Gaussian elimination can be applied to solve for the scattering amplitudes in $O(N^3)$ operations and require $O(N^2)$ filling time of the matrix, where N is the number of unknowns. However, the computation is prohibitively intensive for large objects and the tremendous memory requirement cannot be met by most computers.

Iterative solvers such as CG (conjugate gradient) [13], [14] or BiCG (bi-conjugate gradient) method [15]–[17] can be used to circumvent the matrix storage difficulty although there are still $O(N^2)$ operations in each iteration and total number of iterations to converge is problem-dependent. In this work, we apply BiCG to solve for the solution of the matrix equation iteratively. When an iterative solver is used, the main cost of seeking the solution is the cost of performing a matrix-vector multiplication. When the inhomogeneous body is discretized into a regular grid, however, the resultant equation has a block-Toeplitz structure. Exploiting the block-Toeplitz structure, we can perform the matrix-vector multiplication in $O(N \log N)$ operations by FFT [10]–[12], [18].

The method can be shown to require $O(N)$ memory storage. Hence, it can be used to solve fairly large problems. A volume scattering problem with 90 000 unknowns is solved on a Sparc 10 workstation. It is shown that iterative solvers converge faster for lossy bodies than lossless ones. This is because the matrix condition number for the former cases is smaller than that for the latter ones, as a lossless body could have high Q internal resonance modes.

As the simulation results show, by using the T-matrix formulation, the condition number of the resultant matrix is independent of the mesh size of a uniform grid. Therefore, the number of iterations does not grow when the body is gridded finer in order to achieve better resolution.

II. FORMULATION AND IMPLEMENTATION

When a number of scatterers are placed on a uniform array, their scattering solution can be obtained efficiently by using FFT and an iterative method.

The total field due to an array of nonidentical scatterers can be written as

$$\mathbf{E}(\mathbf{r}) = \boldsymbol{\psi}^t(k_0, \mathbf{r}_s) \cdot \mathbf{a}_s + \sum_{i=1}^{N} \boldsymbol{\psi}^t(k_0, \mathbf{r}_i) \cdot \mathbf{b}_i \qquad (1)$$

where $\mathbf{r}_i = \mathbf{r} - \mathbf{r}_i'$ and $\mathbf{r}_i'$ is the location of the scattering center of the ith scatterer. $\boldsymbol{\psi}^t(k_0, \mathbf{r}_i)$ is a row vector containing the vector spherical harmonics from each scatterer. The first term in (1) comprises the incident field while the second term is the scattered field. The vectors $\mathbf{a}_s$ and $\mathbf{b}_i$ contain the amplitudes of the incident

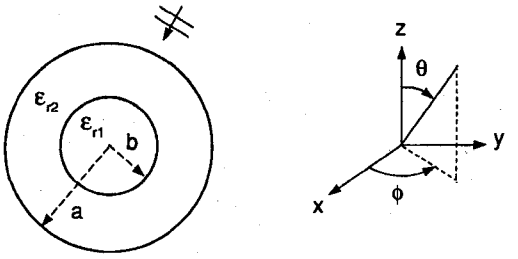

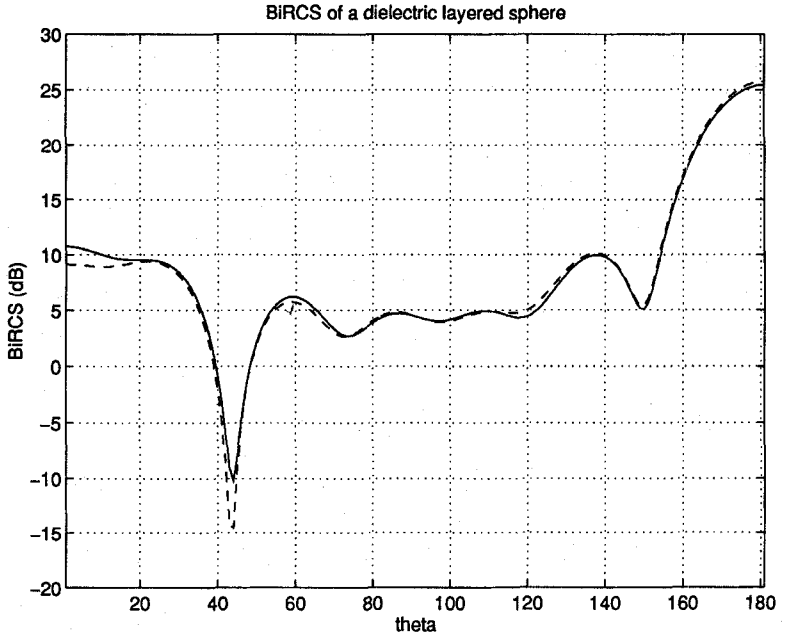

(a)

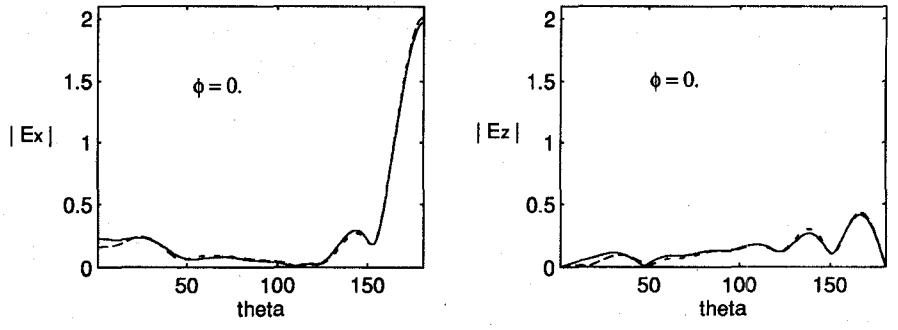

(b)

Fig. 1. (a) The Bi-RCS of a spherically layered sphere. The solid line is from the Mie series solution; the dash line is the numerical solution. Here $b = 0.5\lambda_0$, $\epsilon_{r1} = 1.2$, $a = 1.0\lambda_0$ and $\epsilon_{r2} = 2.4$. A $30 \times 30 \times 30$ grid is used. (b) The near fields of the spherically layered sphere. The observation points are $3\lambda_0$ away from the center. The solid line and dash line denote the Mie series solution and numerical solution, respectively.

field harmonics and the scattered field harmonics from the ith scatterer, respectively.

Focusing on the jth scatterer, we can use the addition theorem or the translation matrix [6], [19] to change the coordinates of all the spherical harmonics to that of the jth scatterer to obtain

$$\mathbf{E}(\mathbf{r}) = \Re g\boldsymbol{\psi}^t(k_0, \mathbf{r}_j) \cdot \overline{\boldsymbol{\alpha}}_{js} \cdot \mathbf{a}_s + \Re g\boldsymbol{\psi}^t(k_0, \mathbf{r}_j) \cdot \sum_{\substack{i=1 \\ i\neq j}}^{N} \overline{\boldsymbol{\alpha}}_{ji} \cdot \mathbf{b}_i + \boldsymbol{\psi}^t(k_0, \mathbf{r}_j) \cdot \mathbf{b}_j. \tag{2}$$

Looking at the above, we see that the first two terms are incident waves impinging on the jth scatterer while the third term is the scattered field off the jth scatterer. Therefore, the amplitude of the third term must be related to the total amplitude of the first two terms via the isolated scatterer T matrix of the jth scatterer, i.e., $\overline{\mathbf{T}}_{j(1)}$. Here, $\overline{\mathbf{T}}_{j(1)}$ is diagonal for the spherical scatterer. Consequently, we have

$$\mathbf{b}_j = \overline{\mathbf{T}}_{j(1)} \cdot \left[\overline{\boldsymbol{\alpha}}_{js} \cdot \mathbf{a}_s + \sum_{\substack{i=1 \\ i\neq j}}^{N} \overline{\boldsymbol{\alpha}}_{ji} \cdot \mathbf{b}_i \right], \quad j = 1, \cdots, N. \tag{3}$$

Essentially, we match the boundary condition at the surface of the jth scatterer instead at the center of the scatterer. This explains why this formulation avoids the singularity problem.

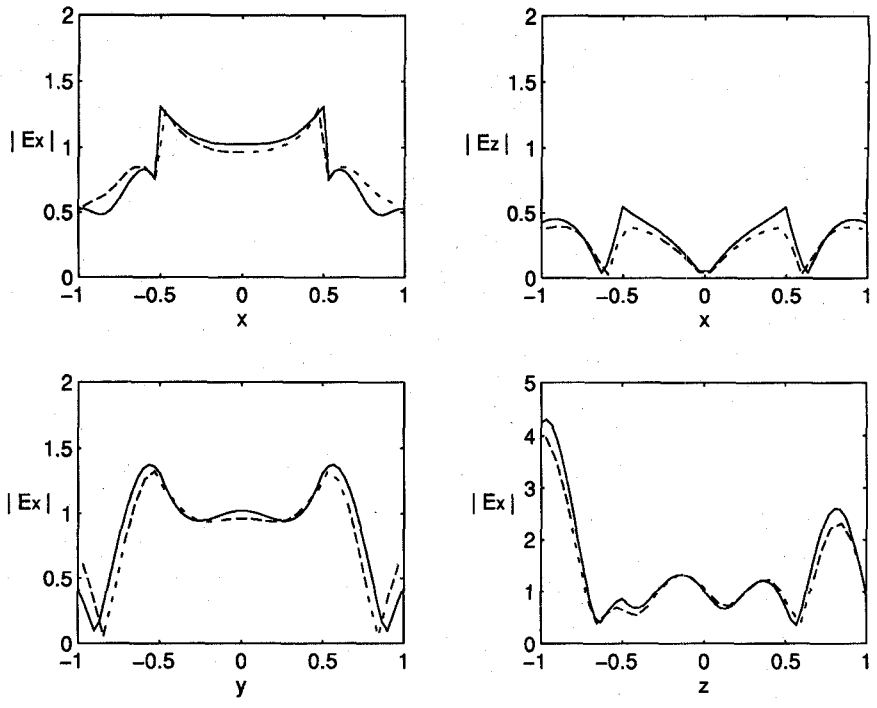

(c)

Fig. 1. *(Continued.)* (c) Different components of the internal fields of the spherically layered sphere are calculated at x, y, and z axes by the Mie series (solid lines) and the algorithm (dashed lines).

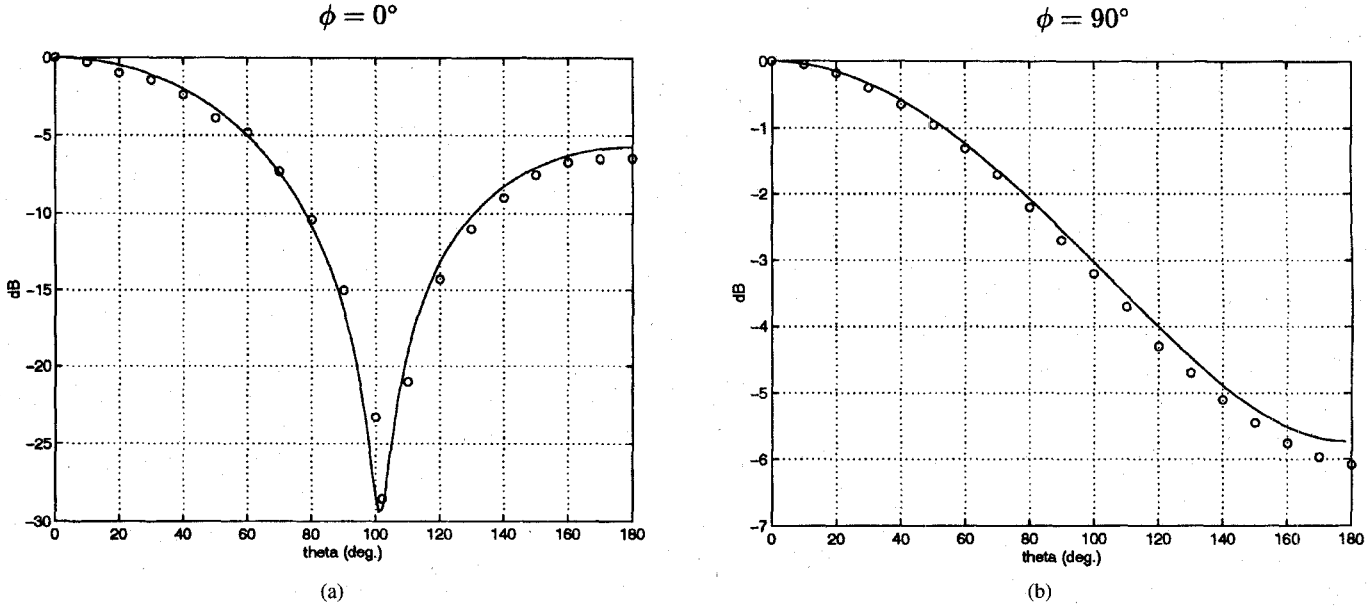

(a) (b)

Fig. 2. The far fields as a function of θ computed for a lossless dielectric cube with $\epsilon_r = 9$ and $k_0 a = 0.628\,319$. The solid lines represent the results by the BiCG-FFT T-matrix method and the symbols ∘ represent the results by Zwamborn and van den Berg. A $7 \times 7 \times 7$ grid is used. (a) The far field $||\mathbf{E}_\theta||$ as a function of θ. (b) The far field $||\mathbf{E}_\phi||$ as a function of θ.

Equation (3) could be rewritten as

$$\mathbf{b}_j - \overline{\mathbf{T}}_{j(1)} \cdot \sum_{\substack{i=1 \\ i \neq j}}^{N} \overline{\boldsymbol{\alpha}}_{ji} \cdot \mathbf{b}_i = \overline{\mathbf{T}}_{j(1)} \cdot \overline{\boldsymbol{\alpha}}_{js} \cdot \mathbf{a}_s \tag{4}$$

or

$$\mathbf{B} - \overline{\mathbf{T}} \cdot \overline{\mathbf{A}} \cdot \mathbf{B} = \overline{\mathbf{T}} \cdot \mathbf{S} \tag{5}$$

where $\overline{\mathbf{T}}$ and $\overline{\mathbf{A}}$ are block matrices, and $\mathbf{B}$ and $\mathbf{S}$ are block vectors whose block elements are given by

$$[\overline{\mathbf{T}}]_{ij} = \delta_{ij} \overline{\mathbf{T}}_{j(1)} \tag{6a}$$

$$[\overline{\mathbf{A}}]_{ij} = \begin{cases} \overline{\boldsymbol{\alpha}}_{ij}, & \text{if } j \neq i \\ 0, & \text{otherwise} \end{cases} \tag{6b}$$

$$[\mathbf{B}]_j = \mathbf{b}_j, \tag{6c}$$

$$[\mathbf{S}]_j = \overline{\boldsymbol{\alpha}}_{js} \cdot \mathbf{a}_s. \tag{6d}$$

Equation (5) can be solved with iterative methods like the bi-conjugate gradient (BiCG) method. It is well known that CG type methods converge to the solution in at most N iterations under exact arithmetics [13], [14] and generally can achieve enough accuracy in much fewer iterations than N. Also, in most cases, the BiCG method converges faster than the CG method, since the former deals

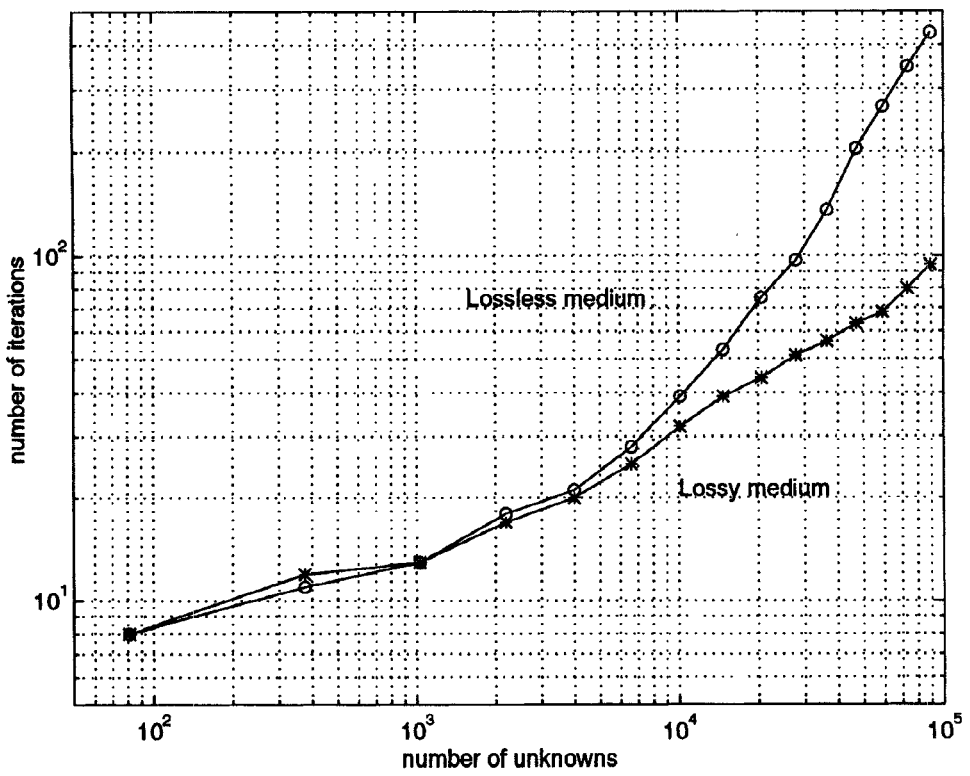

Fig. 3. The number of iterations versus number of unknowns for lossless cubes of $\epsilon_r = 9.0$ and for lossy cubes of $\epsilon_r = 9.0 + i3.0$.

with the matrix equation directly instead of the normal equation in the latter, where the condition number has been squared. In such a method, the major computational cost would be in the matrix-vector multiplication $\overline{\mathbf{A}} \cdot \mathbf{B}$. For a dense matrix, the cost of such a matrix-vector multiplication requires $O(N^2M^2)$ operations, where M is the dimension of the $\overline{\boldsymbol{\alpha}}_{ij}$ matrices.

When the scattering centers are placed on a uniform grid, then $\overline{\boldsymbol{\alpha}}_{ij} = \overline{\boldsymbol{\alpha}}(\mathbf{r}'_i - \mathbf{r}'_j)$. The translation matrix is only a function of $\mathbf{r}'_i - \mathbf{r}'_j$. When the formulation is implemented, the summation in (4) is actually replaced with a three dimensional summation. In such a case, $\overline{\mathbf{A}}$ can be expressed as a block-Toeplitz matrix. By grouping the elements of same harmonics into one block, the block-Toeplitz matrix is converted to a Toeplitz-block matrix (i.e., each block is Toeplitz). Then the fast Fourier transform (FFT) method can be used to expedite the matrix-vector multiplication $\overline{\mathbf{A}} \cdot \mathbf{B}$ with operation count of $O(NM \log N)$.

If the spheres are small compared to λ_0, it possesses only electric dipole moments that correspond to the first three harmonics in $\overline{\mathbf{T}}_{j(1)}$. Therefore, $M = 3$ and, furthermore, there are only six independent elements in the 3×3 matrix $\overline{\boldsymbol{\alpha}}_{ij}$ due to the rotational symmetry.

In order to perform the matrix-vector multiplication more efficiently, the Fourier transform of $\overline{\mathbf{A}}$, $\tilde{\overline{\mathbf{A}}}$ is calculated only once outside the iteration loop and stored. Note that $\overline{\mathbf{A}}$ has been extended to a circulant matrix in the x-, y-, and z-directions and zeros have to be padded to the original vector to prevent aliasing. Hence, whenever a matrix-vector multiplication is required in each iteration, three forward, three-dimensional (3-D) FFT's corresponding to three harmonics are first performed, they are then multiplied by $\tilde{\overline{\mathbf{A}}}$ in the frequency domain, and finally three inverse 3-D FFT's are carried out. Then, the product can be obtained by discarding those entries with zero-padding in the first place.

The memory requirement of the method is still $O(N)$ since each block matrix in $\overline{\mathbf{A}}$ can be represented by one of its rows or columns.

III. Results and Conclusion

In Fig. 1, a dielectric layered sphere is considered. This sphere is approximated by a cluster of small cubes. For those cubes that lie astride two different media, they are assigned to either media according to whether the center of the cube is inside the spherical interface or not. Then, all the cubes are replaced with equivolume spheres. The incident field is a uniform plane wave impinging from $+z$ axis and with x polarization. The BiRCS, near field, and internal field results have been shown in Fig. 1(a)–(c), and they all agree quite well with the Mie series solutions. The BiRCS is defined as

$$\text{BiRCS}\,(\phi, \theta) = 10 \log [\sigma_\infty(\phi, \theta)] - 10 \log (\lambda_0^2)\, dB$$

where

$$\sigma_\infty (\phi, \theta) = \lim_{R \to \infty} 4\pi R^2 \frac{||\mathbf{E}^s(\phi, \theta)||^2}{||\mathbf{E}^i(\phi, \theta)||^2}$$

and in which $||\mathbf{E}^s (\phi, \theta)||^2$ and $||\mathbf{E}^i (\phi, \theta)||^2$ denote the scattered field and incident field vectors, respectively. The algorithm converges in 53 iterations for the case in Fig. 1 and takes about $1\frac{1}{2}$ hours CPU time on Sparc 10 workstation working in double precision. A good agreement is also observed in Fig. 2 for a dielectric cube [12].

Shown in Fig. 3 are the number of iterations versus the number of unknowns for lossless and lossy objects. As we have observed in two-dimenional (2-D) cases [20], the number of iterations increases with the size of the object, and in the lossy medium, fewer iterations are required to converge than in the lossless medium. This shows that in the lossy medium, the complex permittivity shifts the otherwise small eigenvalues in the lossless medium away from the origin. Physically, the resonant frequencies of the lossy dielectric body are complex, while in practice, the operating frequency is always real, which precludes the eigenvalues from being too close to zero.

The number of iterations is approximately proportional to N for lossless objects and seemingly to $N^{0.75}$ for lossy ones when N is large. Without preconditioners, the eigenvalue distribution

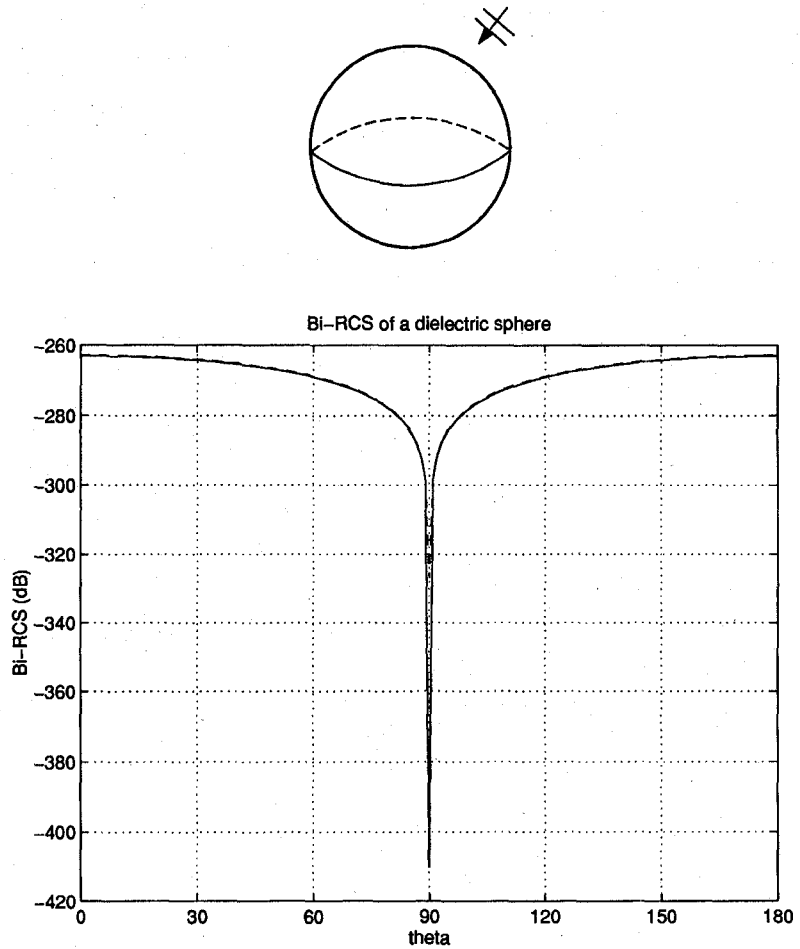

Fig. 4. The Bi-RCS of a dielectric sphere. The solid line is from the Mie series solution; the dash line is the numerical solution. Here, the radius = $10^{-5}\lambda_0$ and $\epsilon_r = 4.0$. A $16 \times 16 \times 16$ gird is used.

seems dispersive without confinement as N grows and the erratic convergence of BiCG algorithm worsens the already poor condition number. In order for BiCG-FFT or its like to be more favorable, a suitable preconditioner is needed.

Finally, we demonstrate that when the object is gridded finer, the T-matrix formulation is still stable. The first example is a homogeneous dielectric sphere with $\epsilon_r = 4.0$ and the radius $= 10^{-5}\lambda_0$. The simulation results show that the number of iterations remains as six for the cases of $8 \times 8 \times 8$, $16 \times 16 \times 16$, and $32 \times 32 \times 32$ grids. Fig. 4 shows one of the results and it agrees very well with the exact solution. We have also run a second example (not shown here) that is a homogeneous dielectric cube with $\epsilon_r = 9.0$ and the side length $= 0.34\lambda_0$. Similar to the first example, the number of iterations is 16 for all the three different grids as mentioned above.

REFERENCES

[1] J. H. Richmond, "Scattering by a dielectric cylinder of arbitrary cross section shape," *IEEE Trans. Antennas Propagat.*, vol. 13, pp. 334–341, 1965.

[2] D. E. Livesay and K. M. Chen, "Electromagnetic fields induced inside arbitrarily shaped biological bodies," *IEEE Trans. Microwave Theory Tech.*, vol. 22, no. 12, pp. 1273–1280, 1974.

[3] T. C. Guo and W. W. Guo, "Scattering of vector waves by arbitrary three-dimensional dielectric objects," in *Proc. 1987 Inter. Micro. Symp.*, Rio de Janeiro, Brazil, July 1987, pp. 307–312.

[4] T. C. Guo, W. W. Guo, and H. N. Oguz, "A technique for three-dimensional dosimetry and scattering computation of vector electromagnetic fields," *IEEE Trans. Magn.*, vol. 29, no. 2, pp. 1636–1641, 1993.

[5] ——, "A matrix formulation of dielectric imaging, dosimetry and computation of vector electromagnetic field," in *Proc. Fifth Biennial IEEE Conf. in Electromagnetic Field Computation,* Monterey, CA, Mar. 22–26, 1993, pp. 413–423.

[6] Y. M. Wang and W. C. Chew, " A recursive of T-matrix approach for the solution of electromagnetic scattering by many spheres," *IEEE Trans. Antennas Propagat.*, vol. 41, no. 12, pp. 1633–1639, 1993.

[7] P. C. Waterman, "Matrix formulation of electromagnetic scattering," *Proc. IEEE,* vol. 53, pp. 805–811, 1965.

[8] W. C. Chew, *Waves and Fields in Inhomogeneous Media.* New York: Van Nostrand Reinhold, 1990.

[9] R. H. Harrington, *Field Computations by Moment Methods.* New York: McGraw-Hill, 1968.

[10] D. T. Borup and O. P. Gandhi, "Fast-Fourier transform method for the calculation of SAR distribution in finely discretized models of biological bodies," *IEEE Trans. Microwave Theory Tech.*, vol. 32, no. 4, pp. 355–360, 1984.

[11] C. Y. Shen, K. J. Glover, M. I. Sancer, and A. D. Varvatsis, "The discrete Fourier transform method of solving differential-integral equations in scattering theory," *IEEE Trans. Antennas Propagat.*, vol. 37, no. 8, pp. 1032–1041, 1989.

[12] A. P. M. Zwamborn and P. M. van den Berg, "The three-dimensional weak form of the conjugate gradient FFT method for solving scattering problems," *IEEE Trans. Microwave Theory Tech.*, vol. 40, no. 9, pp. 1757–1766, 1992.

[13] M. R. Hestenes and E. Stiefel, "Methods of conjugate gradient for solving linear systems," *J. Research of the National Bureau of Standard,* vol. 49, pp. 409–435, 1952.

[14] O. Axelsson and V. A. Barker, *Finite Element Solution of Boundary Value Problems.* New York: Academic, 1984.

[15] C. Lanczos, "An iteration method for the solution of the eigenvalue problem of linear differential and integral operators," *J. Research of the National Bureau of Standard,* vol. 45, pp. 255–282, 1950.
[16] R. Fletcher, "Conjugate gradient methods for indefinite systems," in *Numerical Analysis Dundee 1975,* G. A. Watson, Ed. New York: Springer-Verlag, 1976, pp. 73–89.
[17] T. K. Sarkar, "On the application of the generalized bi-conjugate gradient method," *J. Electromagn. Waves Appl.,* vol. 1, no. 3, pp. 223–242, 1987.
[18] M. F. Cátedra, J. G. Cuevas and L. Nuño, "A scheme of analyze conducting plates of resonant size using the conjugate-gradient method and the fast Fourier transform," *IEEE Trans. Antennas Propagat.,* vol. 36, no. 12, pp. 1744–1752, 1988.
[19] W. C. Chew, "Recurrence relation for three dimensional scalar addition theory," *J. Electromagn. Waves Appl.,* vol. 6, no. 2, pp. 133–142, 1992.
[20] J. H. Lin and W. C. Chew, "A comparison of the CG-FFT method and the recursive aggregate T-matrix algorithm," in *IEEE Antennas Propagat. Soc. Int. Symp. Dig.,* 1992, pp. 1591–1594.

Reduced Invasiveness of Noncontact Electrooptic Probes in Millimeter-Wave Optoelectronic Characterization

A. Zeng, S. A. Shah, and M. K. Jackson

***Abstract*—We report time-resolved measurements of the invasiveness of $LiTaO_3$ external probes in millimeter-wave electrooptic sampling. Using external probe tips at varying distances from a coplanar stripline, we show that invasiveness can be reduced in a noncontact configuration at the expense of measurement sensitivity. In the contact configuration, the risetime can be significantly lengthened by dispersion and signal reflection caused by the probe tip.**

I. Introduction

Electrooptic sampling (EOS) has been used in characterization of high-speed electronic devices [1]–[3]. Many of these measurements were made using $LiTaO_3$ external probes. To date there have been a limited number of experimental studies of the invasiveness of $LiTaO_3$ probes. The effects of reflection between the top and bottom interfaces of the $LiTaO_3$ crystal on amplitude measurement has been studied by Frankel *et al.* [4]. The effect of probe-tip-induced dispersion on risetime measurements has been studied by putting a dummy $LiTaO_3$ crystal between the electrical signal generator and the probe site [1]. In both of these studies the $LiTaO_3$ probes were placed in direct contact with the transmission line electrodes and the measurements were performed in the time domain. The invasiveness of external probes has also been studied using internal electrooptic sampling, where a dummy probe was placed in the vicinity of the electrodes of a coplanar stripline driven by a microwave synthesizer [5], [6]. Theoretical studies of the invasiveness of electrooptic probes have been reported [7], [8].

In this paper, we report a study of the invasiveness of external $LiTaO_3$ probes, extending previous measurements to higher frequencies and lower invasiveness. We show that contact electrooptic sampling can lead to measurement error. We also show that noncontact electrooptic sampling provides a more accurate measurement of risetime, at the expense of reduced sensitivity.

Manuscript received February 22, 1995; revised March 20, 1996. This work was supported in part by the Natural Sciences and Engineering Research Council of Canada (NSERC) under individual research grants and networks of centers of excellence (Micronet) programs as well as fellowship support from the University of British Columbia and NSERC.

The authors are with the Department of Electrical Engineering, University of British Columbia, Vancouver, BC V6T-1Z4, Canada.

Publisher Item Identifier S 0018-9480(96)04721-7.

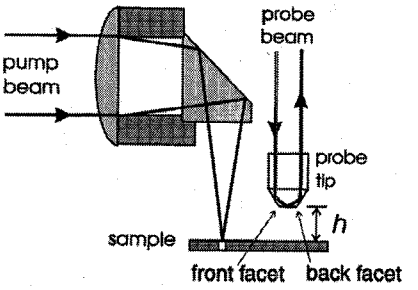

Fig. 1. Schematic of the pump and probe optics. The air gap h between the tip and the sample can be adjusted.

II. Experiment

Electrooptic measurements are made with 150-fs pulses from a mode-locked Titanium-Sapphire laser. The external probe has an inverted pyramid shape, with a $LiTaO_3$ crystal of footprint 200 μm square and thickness 20 μm at the bottom. The arrangement of pump and probe optics and the sampling tip is shown in Fig. 1; the probe is used in a total-internal-reflection configuration, and the probe-sample spacing h can be adjusted. Imaging of interference fringes under the probe tip is used as a indication of probe tip parallelism with respect to the sample surface, which is essential to ensure good contact. The sample is a coplanar stripline with 50-μm-wide electrodes and 5-μm spacing deposited on a 500-μm-thick semi-insulating GaAs substrate. A photoconductive switch incorporated in the transmission line is used to generate step like pulses.

III. Results

In Fig. 2, we show waveforms measured with two different air gaps, and at two different positions of the probe beam in the sampling tip; the probe is approximately 1.5 mm from the photoconductive switch. In Fig. 2(a), we show results for $h = 0$ (contact); the solid line shows the waveform measured with the probe beam positioned near the facet closest to the photoconductive switch, which we will refer to as the front facet. The risetime of the signal is 1.9 ps. The dashed line in Fig. 2(a) shows the waveform measured with the probe beam near the back facet; the risetime in this case is 2.1 ps. In Fig. 2(b), we show similar measurements for an air gap of $h = 10\,\mu$m. The solid line measured at the front facet has a risetime of 1.7 ps, which is the same as the risetime of the signal measured at the back facet, shown by a dashed line.

The differences between the risetimes seen in Fig. 2(a) are not due to the usual dispersion on the undisturbed transmission lines; we have made measurements of risetime at varying distances along the transmission line that show no significant difference in risetime over the same distance. We attribute the lengthening in risetime to the increased dispersion and attenuation introduced by the $LiTaO_3$ probe, which functions as a superstrate. In Fig. 2(a), the feature near 14 ps in the curve measured near the front facet is due to reflection from the back facet of the probe, because of the large mismatch caused by the differing impedances of the transmission lines with and without the $LiTaO_3$ superstrate. The same reflection is not as obvious in the